Progress In Electromagnetics Research C, Vol. 115, 187–203, 2021

Design of Compact CPW-Fed Symmetrical Staircase-Shaped UWB Antenna Using Transmission Line Model

Budhadeb Maity[1, *] and Sisir K. Nayak[2]

Abstract—A co-planar waveguide-fed symmetrical staircase-shaped ultra-wideband antenna is proposed in this work. This antenna consists of three pairs of rectangular notches, two symmetrical C-shaped slots and two pairs of quarter-circular-ring-slits which are etched on the rectangular radiator and ground plane, respectively. By sequentially inserting three pairs of rectangular notches with proper positions, an excellent impedance bandwidth of 1.55–16.95 GHz (166.51%), i.e., a 10.94 : 1 ratio bandwidth is obtained. The total volume of the prototype is merely $0.239 \times 0.224 \times 0.004\lambda_l^3$, λ_l wavelength of the free space at the lowest operating frequency (i.e., 1.55 GHz). As a result, wider impedance bandwidth, fair gain, and better impedance matching of the proposed antenna are obtained. It is observed that the simulation results are in good agreement with the measurement results. The transmission line model (TLM) of the proposed antenna is presented, and it shows the antenna behavior based on the effect of each element. It is observed that the characteristics of the TLM model are close to the simulation result using the CST simulator. The prototype is successfully implemented, fabricated, and compared with the experimental results.

1. INTRODUCTION

Printed microstrip slot antennas are widely adopted in wireless communications systems due to the advantages such as light weight, low profile, low cost, and easy integration with monolithic microwave integrated circuits (MMIC). However, the use of microstrip slot antennas brings a new problem, i.e., narrow bandwidth, which is important to the fidelity of ultra-wideband (UWB) signals. Compared to microstrip antennas coplanar waveguide (CPW)-fed antennas offer relatively broad bandwidth, high-speed data rate, low sensitivity to fading, flexibility, allow the integration with surface-mount devices, and can be used for UWB antennas operation [1, 2]. But in modern wireless communications, there is a significant increase in the demand for various CPW-fed printed antennas with wider bandwidth and miniaturized size. The monopole and Vivaldi antennas having wide bandwidth and good radiation are extensively used as reported in [3]. Monopole antennas are installed perpendicularly to carriers, and a Vivaldi antenna needs a tapered slot, so in both cases a relatively large area is required.

In recent years, for the requirement of enhanced impedance bandwidth, slot antenna has been further developed. A large number of designs have been proposed in a compact size and enhanced bandwidth [4–9]. In [4], the length of the central metallic strip line is stretched beyond the CPW plane to achieve an improved radiation performance like the monopole antenna. Similarly, the central strip plays a significant role in finding the wider bandwidth with the subsequent creation of different shapes such as CPW-fed antennas with a dual-reverse-arrow fractal structure [5], flexible bow-tie slot antenna [6], rose-curve shape monopole antenna [7], wideband fractal shapes structure [8], etc. Although the wideband

Received 30 July 2021, Accepted 6 September 2021, Scheduled 18 September 2021

* Corresponding author: Budhadeb Maity (maity176151008@iitg.ac.in).

[1] School of Energy Science and Engineering, Indian Institute of Technology Guwahati, Guwahati, Assam 781039, India. [2] Department of Electronics and Electrical Engineering, Indian Institute of Technology Guwahati, Guwahati, Assam 781039, India.

fractal shapes structure antenna is capable of providing wider impedance bandwidth performance, the size of this antenna is large.

The compactness is the major necessity for today's wireless applications devices, e.g., UWB applications and for this encouraging the exploration in the direction of smaller size CPW-fed tapered-slot structures [9]. Since the bandwidth of traditional slot antennas is confined by slot width, the operation bandwidth is not easily enhanced [10]. UWB and compact antennas are presented in [11–19]. In [11], a semi-elliptically fractal slot patch antenna with an asymmetrical ground plane, having an impedance bandwidth of 172% is proposed. However, the dimension is $77 \times 35\,\text{mm}^2$. A Y-shaped central monopole meandered-slot miniature antenna structure is used for wider bandwidth in [12]. The antennas proposed in [13–15], with a printed E-shape slot, an arc shape stub, and fishtail-shape different from other coplanar waveguide-fed slot antennas, are used only for exciting the slot which has a very good impedance bandwidth. A Vivaldi antenna uses a stepped connection structure to enhance the impedance bandwidth and the matched antenna feed [16]. In [17], a microstrip line-fed hybrid monopole antenna which is electromagnetically coupled band-notched is presented. In [18], the change of lower and upper resonant frequencies with respect to the width of a U-slot and the existence of only modes 1 and 3 due to the capacitive effect with respect to U-slot patch structure are discussed. Besides, a wide bandwidth and compact size UWB slot antenna different from the traditional wideband slot antennas is proposed [19].

In this work, considering the enhanced impedance bandwidth (BW), gain, and compact size, a CPW-fed symmetrical staircase-shaped UWB antenna is presented. Since the design and the fabricated antenna has a symmetrical pair of C-shaped slots, two pairs of quarter-circular-ring-slits (QCRSs), and three pairs of rectangular notches which are sequentially embedded in bottom corners of the rectangular patch, five resonant peaks, i.e., 2.31, 4.85, 8.33, 12.11, and 16.41 GHz are achieved. As a result, the proposed antenna has wider impedance bandwidth, better impedance matching, a high value of bandwidth dimension ratio (BDR) compared to the antennas presented in [5, 7, 11, 13, 14, 17, 18, 20], and the stability of E- and H-plane is obtained. Then, an equivalent transmission line model (TLM) of the proposed antenna is developed. An optimization is used in Applied Wave Research (AWR) simulator to find the circuit parameters such as resistance (R), inductance (L), and capacitance (C) of the TLM equivalent circuit using the S_{11} simulated parameters [20–22] of the proposed antenna.

This paper is organized as follows. Section 2 states the design steps and enhancement in impedance bandwidth and the impedance matching of the proposed antenna. Section 3 gives the parametric studies and BDR of the antenna. Section 4 discusses the TLM-RLC circuit model. The prototype and measured and simulated results are presented and compared in Section 5. Finally, Section 6 presents a brief conclusion to this work.

2. ANTENNA DESIGN

2.1. Antenna Configuration

The structure of the proposed co-planar waveguide-fed symmetrical staircase-shaped (SSS) antenna with enhanced bandwidth is depicted in Figure 1. A wider impedance bandwidth and higher gain performances are achieved by cutting SSS and symmetrical two C-slots on the rectangular radiator. The antenna is fabricated on a $46.32 \times 43.48\,\text{mm}^2$ ($L_s \times W_s$) Rogers (RT/5880) substrate with a thickness of 0.8 mm, dielectric constant of $\epsilon_r = 2.2$, and loss tangent of 0.0009. The electromagnetic software CST is used for simulation. The specific dimensions of the proposed UWB antenna are given in Table 1.

2.2. Design Evolution and Enhanced Bandwidth

The evolutions for designing the antennas are summarized in five steps as follows. First Step: The evolution steps of the antenna design are shown in Figure 2. Antenna 1 is a CPW-fed simple rectangular patch antenna whose simulated S_{11} results are presented in Figure 3. It is observed from Antenna 1 that the impedance bandwidth performance is from 8.35 to 11.45 GHz (normalized bandwidth 31.31%). It shows only one resonance band (it cannot provide better characteristics performance of $S_{11} \leq -10\,\text{dB}$)

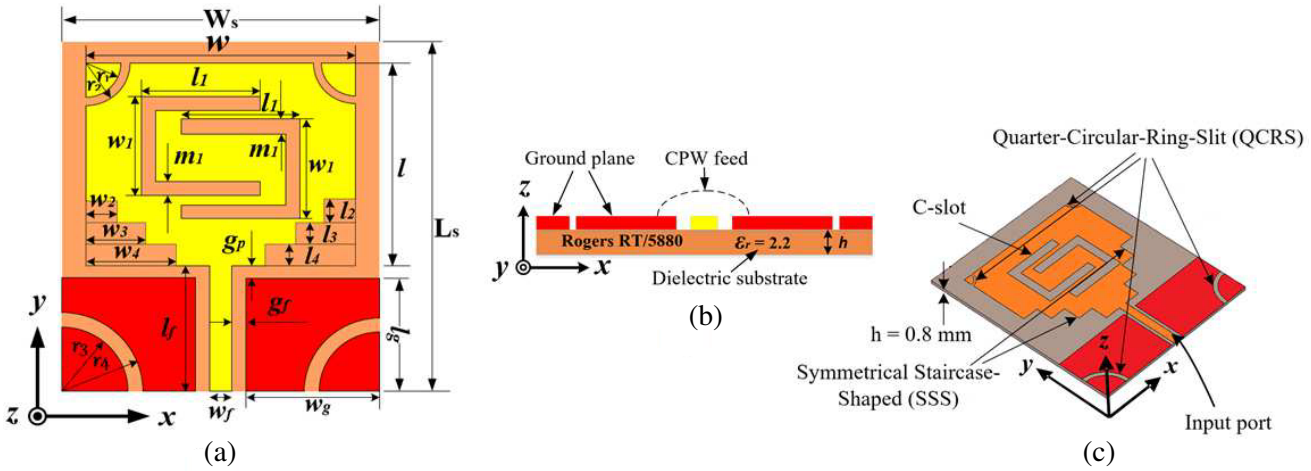

Figure 1. Geometry of the proposed CPW-fed symmetrical staircase-shaped UWB antenna, (a) top view, (b) front view and (c) configuration in three dimensions.

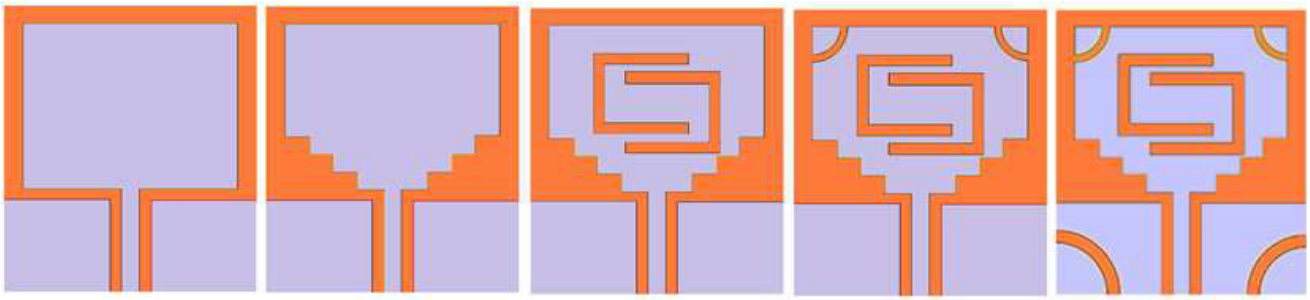

Figure 2. Evolution of the proposed symmetrical staircase-shaped UWB antenna, (a) Antenna 1 (simple rectangular), (b) Antenna 2, (c) Antenna 3, (d) Antenna 4 and (e) Antenna 5 (proposed).

Table 1. Geometric parameters of the proposed antenna.

Parameter	Units (mm)	Parameter	Units (mm)	Parameter	Units (mm)
L_s	46.32	w_2	3.99	w_f	2
W_s	43.48	w_3	7.97	w_g	20
l	28.52	w_4	11.95	l_g	12.9
w	33.88	m_1	2	r_1	2
l_1	13.95	g_p	1.9	r_2	2.4
l_2, l_3, l_4	3.99	g_f	0.74	r_3	5.75
w_1	12	l_f	14.8	r_4	6.75

due to the external current path, and its frequency can be expressed as [12]:

$$f_{ext} \approx \frac{c}{\sqrt{\epsilon_{eff}} L_{\text{path}}} \tag{1}$$

where L_{path} is the external path length, c the speed of light in a vacuum, and ϵ_{eff} the effective dielectric constant.

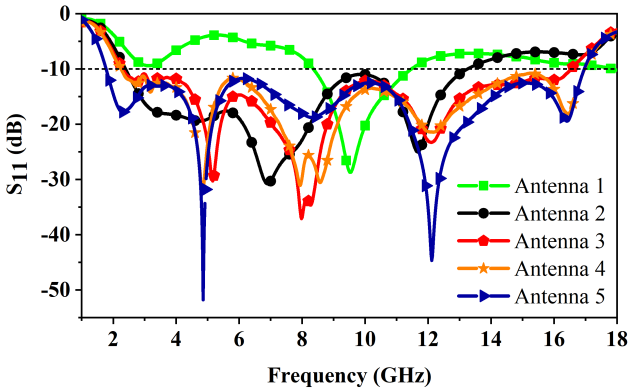

Figure 3. Reflection coefficients versus frequency characteristics for different structures of design antenna.

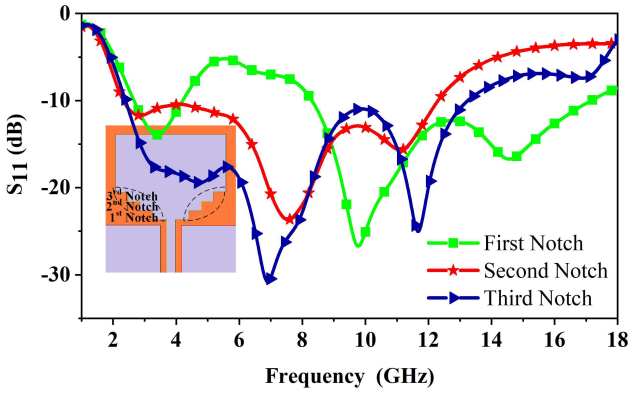

Figure 4. Simulated S_{11} performance of the symmetrical staircase-shaped Antenna 2.

Second Step: The three pairs of notches are sequentially introduced with dimensions of $w_2 \times l_2$, $w_3 \times l_3$, and $w_4 \times l_4$ to generate the frequency of the peak resonant at 6.9 GHz and 11.68 GHz. A wide bandwidth, i.e., 2.40–13.24 GHz (normalized bandwidth 138.62%) and better return loss performances are achieved by inserting the first, second, and third pairs of notches as shown in Figure 4.

Third Step: A conventional symmetrical two C-shaped slot patch antenna with parameters w, l, h, l_1, m_1, and w_1 is designed by using the approximate formulae [27, 28]:

$$w = \frac{c}{2f_r}\sqrt{\frac{2}{\epsilon_r + 1}} \tag{2}$$

$$l = \frac{c}{2f_r\sqrt{\epsilon_{eff}}\sqrt{\mu_o\epsilon_o}} - 2\Delta l \tag{3}$$

where l and Δl are the actual length and effective length of the patch respectively, and ϵ_{eff} is expressed as:

$$\epsilon_{eff} = \frac{\epsilon_r + 1}{2} + \frac{\epsilon_r - 1}{2}\left(1 + 12\frac{h}{w}\right)^{-1/2} \tag{4}$$

$$\Delta l = 0.412h\frac{(\epsilon_{eff} + 0.3)\left(\frac{w}{h} + 0.264\right)}{(\epsilon_{eff} - 0.258)\left(\frac{w}{h} + 0.8\right)} \tag{5}$$

$$w_1 = \frac{c}{f_r\sqrt{\epsilon_{eff}}} - 2(l + 2\Delta l - m_1) \tag{6}$$

$$m_1 = \frac{\lambda_r}{60} \tag{7}$$

where λ_r is the wavelength in vacuum

$$\frac{l_1}{w} \geq 0.3, \quad \frac{l_1}{w_1} \geq 0.75 \tag{8}$$

$$h \geq 0.06\frac{\lambda_r}{\sqrt{\epsilon_r}} \tag{9}$$

where $f_r (= 2.5\,\text{GHz})$ is the designed antenna resonant frequency.

A pair of symmetrical C-slots is introduced at the center on the radiating patch to generate the five peak resonant frequencies at 2.76, 5.16, 7.98, 12.09, and 16.13 GHz, respectively, of Antenna 3. Due to the introduction of C-slots, the improvement in the return loss and impedance bandwidth from 2.32 to 16.52 GHz (BW = 150.74%) (Figure 3) is achieved.

Fourth Step: In the fourth evolution of the antenna (Antenna 4), a pair of symmetrical QCRSs to Antenna 3 is introduced to improve the S_{11} (slightly improved the bandwidth 2.25 GHz–16.96 GHz and percentage of bandwidth 153.15%) performance as shown in Figure 3. From the S_{11} performance, it is observed that five peak resonant frequencies, i.e., 4.84, 7.94, 8.58, 12.18, and 16.44 GHz, are achieved. For further improvement in gain, return loss, and impedance bandwidth, Antenna 4 is modified in step five.

Fifth Step: In the final design Antenna 5, a pair of the symmetrical quarter-circular-ring-slits is introduced on both sides of the ground plane of Antenna 4 to improve S_{11} further. From the S_{11} parameter, it is observed that the excellent impedance bandwidth from 1.77 to 16.96 GHz (normalized bandwidth 162.2%) is achieved. From the S_{11} performance, we have observed five peak resonant frequencies, i.e., 2.31, 4.85, 8.33, 12.11, and 16.41 GHz, and the approximate expression of these frequencies are given as follows:

$$f_{rp1} \cong \frac{c}{2\sqrt{\epsilon_{eff}}(2l_1 + w_1 - m_1)} \tag{10}$$

$$f_{rp2} \cong \frac{c}{2\sqrt{\epsilon_{eff}}(l_1 + w_1 - 2m_1)} \tag{11}$$

$$f_{rp3} \cong \frac{c}{\sqrt{\epsilon_{eff}}(l_1 + w_1 - m_1)} \tag{12}$$

$$f_{rp4} \cong \frac{c}{2\sqrt{\epsilon_{eff}}(l_4 + w/2 - w_4 - w_f/2)} \tag{13}$$

$$f_{rp5} \cong \frac{c}{\sqrt{\epsilon_{eff}}(l_4/2 + w/2 - w_4 - w_f/2)} \tag{14}$$

The electric field distributions of the designed antenna at these peak resonant frequencies are shown in Figure 5. As seen, the first, second, and third peak resonant frequencies are generated by the slots, while the fourth and fifth peak resonant frequencies are generated by the rectangular patch. Table 2 presents a comparison between theoretical and simulated results of peak resonant frequencies of the designed antenna.

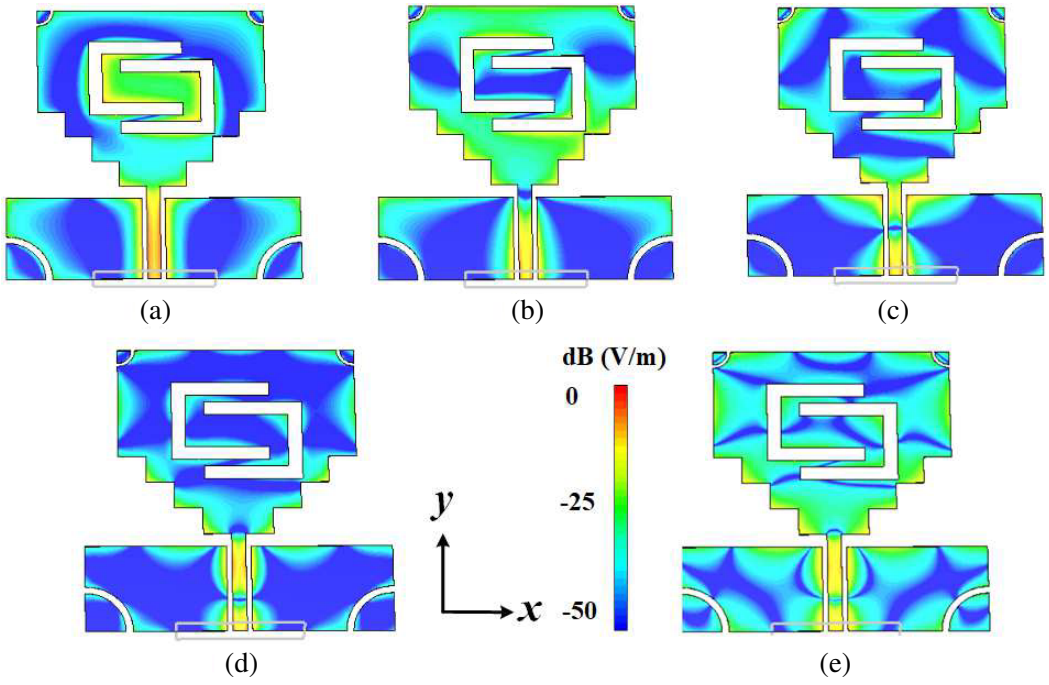

Figure 5. An electric field distribution of the proposed antenna on the slot and conductor at (a) 2.31 GHz, (b) 4.85 GHz, (c) 8.33 GHz, (d) 12.11 GHz and (e) 16.41 GHz.

Table 2. Comparison between theoretical and simulation results of peak resonant frequencies.

Name	f_{rp1} (GHz)	f_{rp2} (GHz)	f_{rp3} (GHz)	f_{rp4} (GHz)	f_{rp5} (GHz)
Simulation	2.31	4.85	8.33	12.11	16.41
Theoretical	2.468	4.672	8.445	12.672	16.911
% Error	6.61	3.78	1.37	4.51	3.00

f_{rp1} ... f_{rp5}: First, second, third, fourth and fifth peak resonant frequencies.

The impedance bandwidth behaviour of the proposed antenna is shown in Figure 6, where the best impedance match is obtained from the proposed antenna (about 162.2% impedance bandwidth). The simulated peak resonant frequencies and their corresponding impedances are presented in Table 3.

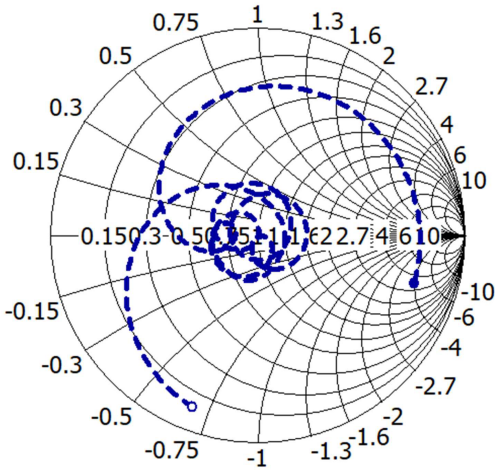

Figure 6. Proposed antenna simulated result of the impedance matching.

Table 3. Simulated peak resonant frequencies and corresponding impedances of the proposed antenna.

Resonant	Simulation frequency (GHz)	Impedance (Ω)
First	$f_{rp1} = 2.31$	$Z_1\ (f_{rp1}) = 100.072 + j2.742$
Second	$f_{rp2} = 4.85$	$Z_1\ (f_{rp2}) = 77.771 + j0.357$
Third	$f_{rp3} = 8.33$	$Z_1\ (f_{rp3}) = 72.499 - j16.679$
Fourth	$f_{rp4} = 12.11$	$Z_1\ (f_{rp4}) = 77.504 - j0.897$
Fifth	$f_{rp5} = 16.41$	$Z_1\ (f_{rp5}) = 62.392 + j0.986$

3. PARAMETRIC ANALYSIS

3.1. Effect of l_1, w_1 and m_1 of C-Slots

In Figure 1(a), the symmetrical C-slots have horizontal slot l_1, vertical slot w_1, and thickness m_1. Figure 7(a) shows the simulated S_{11} performance with the variation of C-slot l_1. It is observed from the S_{11} results that the upper and lower side-band frequencies are affected due to the horizontal slot length of the C-slot of the proposed antenna. More specifically, an increase in length l_1 of the slot from 13.05 to 14.35 mm reduces return loss performance as well as bandwidth. It is also observed that the wideband performance is reduced with a further increase in length l_1 from 13.95 to 14.35 mm. The wider impedance bandwidth of 164.52% is achieved when length $l_1 = 13.95$ mm. The impact of the length

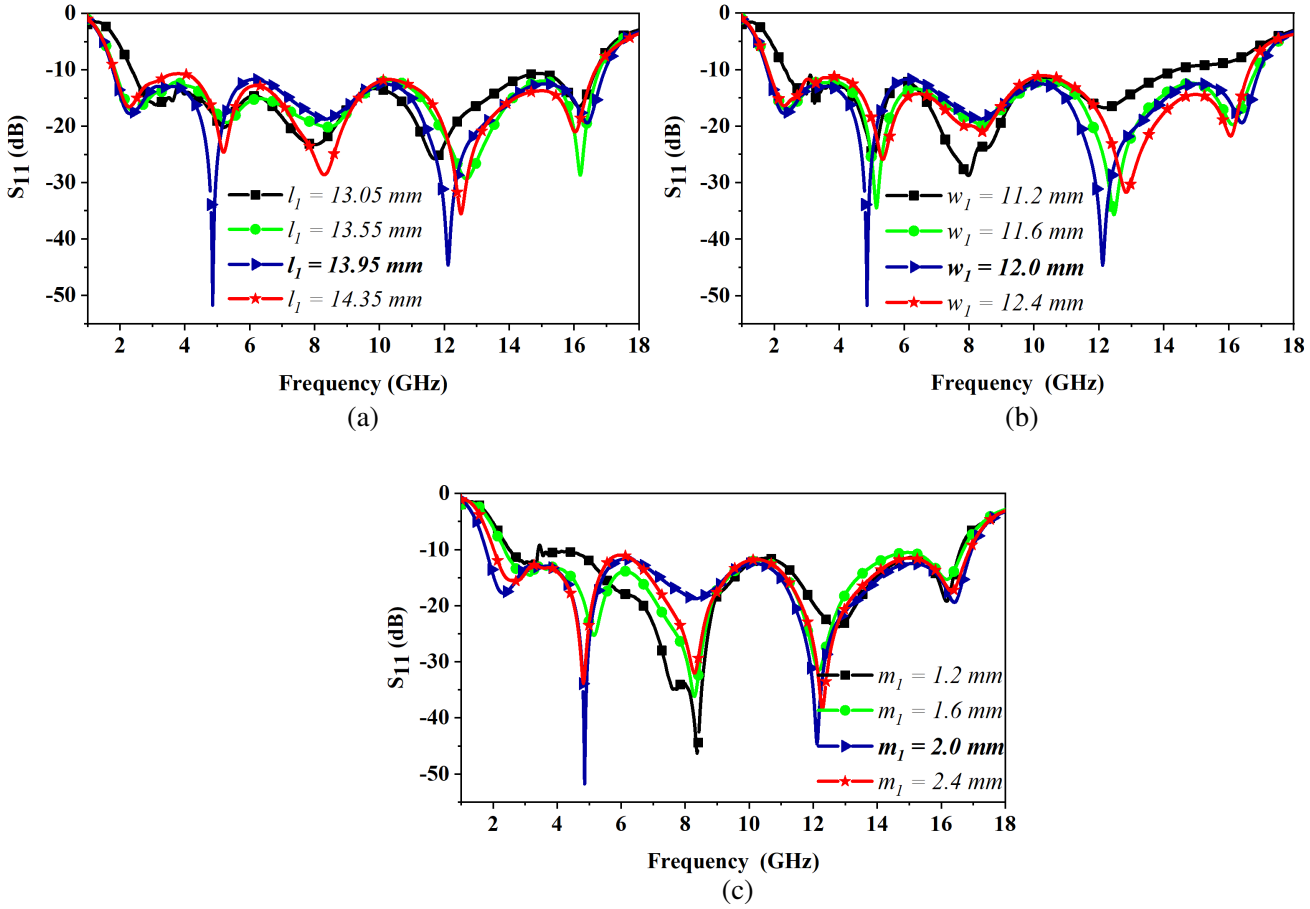

Figure 7. Simulated S_{11} results with different values of C-slot at (a) length l_1, (b) width w_1, and thickness m_1.

of the vertical slot, w_1 from 11.2 to 12.4 mm, is shown in Figure 7(b) where w_1 varies from 11.2 to 12.4 mm. It is observed that with increase in w_1, the upper side-band frequency decreases slightly, but when w_1 decreases the upper and lower side-band frequencies are greatly affected. For good wideband operation, the vertical slot length $w_1 = 12$ mm is more suitable due to its low cross polarization level and stable radiation patterns.

Figure 7(c) shows the S_{11} performance with a variation of m_1 from 1.2 to 2.4 mm. It is observed that the first and second peak resonances shift to higher frequencies with a decrease of m_1. As m_1 increases, the capacitance C_{eq} of the C-shape slot decreases which in turn decreases the propagation constant β (i.e., $\beta \propto \sqrt{C_{eq}}$), as a result, decreases the effective dielectric constant $\sqrt{\epsilon_{eff}} = \beta/C_{eq}$. The guided wavelength $\lambda_g = \lambda_0/\sqrt{\epsilon_{eff}}$ satisfies the resonance condition when the length of the radiating slot is kept constant. It is observed from figure at $m_1 = 2.0$ mm that the proposed antenna shows a wider bandwidth (i.e., 1.77–16.96 GHz).

3.2. Coupled Mode Theory (CMT)

Coupled mode theory (CMT) is a physical phenomenon of coupled transmission line theory [23, 24]. In this theory, a system of two coupled resonators can be analyzed as the superposition of two modes with lower and higher frequencies wherein the resonators move in-phase and anti-phase, respectively. In the present study, ω_+ and ω_- given below are the coupled mode frequencies and uncoupled mode

frequencies, respectively [25].

$$\omega_{\pm} = \omega_o \pm \sqrt{\left(\frac{\omega_2 - \omega_1}{2}\right)^2 + |K|^2} \tag{15}$$

where $\omega_o = (\omega_2 + \omega_1)/2$ and K represents an un-normalized coupling coefficient. Given $\omega_1 = \omega_2$, a normalized coupling coefficient calculated [26] is given as follows:

$$k = \frac{\omega_+^2 - \omega_-^2}{\omega_+^2 + \omega_-^2} \tag{16}$$

Putting Eq. (15) with $\omega_1 = \omega_2$ into Eq. (16), give $k = (2\omega_o K)/(\omega_o^2 + K^2)$. Given $K^2 \ll \omega_o^2$, we have

$$K \sim \omega_o k/2 \tag{17}$$

In the proposed antenna, the simulated surface current distributions on the surface of the radiating patch at five peak resonant frequencies 2.31, 4.85, 8.33, 12.11, and 16.41 GHz are shown in Figure 8. It is also observed from the figure that the lower and higher modes exist near their resonance frequencies. The more charge accumulation on the surface of the patch and the C-shaped slots is noticed as a result, the parameters l_1, w_1 and m_1 controlling the first, second, and third peak resonant frequencies as shown in Figure 8(a), Figure 8(b), and Figure 8(c). The current distributions on the three pairs of the notches are high compared to other parts of the patch element as shown in Figures 8(d) and 8(e). As a result, the geometrical parameters $w_2 \times l_2$, $w_3 \times l_3$, $w_4 \times l_4$, l_1, m_1, and parameters of the QCRS for all the regions of the antenna play an important role in controlling the fourth and fifth peak resonant frequencies. Since the distributions of charges in the rectangular patch and C-shaped slots are in phase at the lower mode and anti-phase at the higher mode, the CMT is relevant to the C-shaped slots.

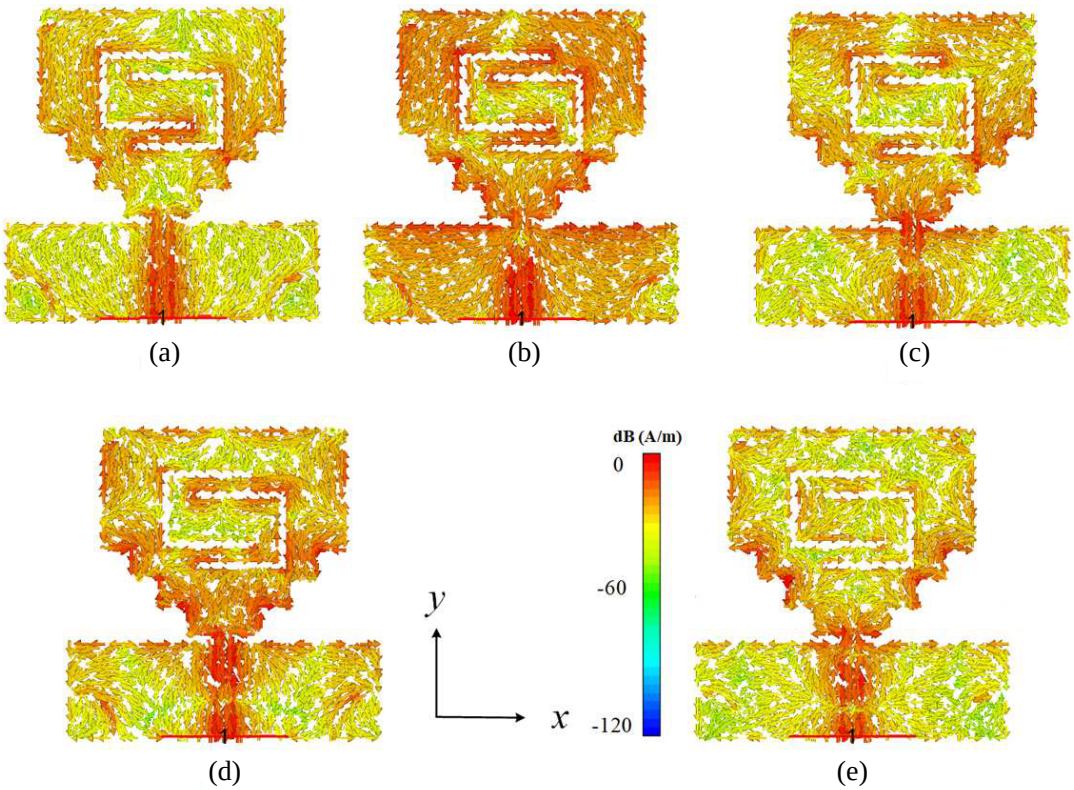

Figure 8. Simulated current distributions of the proposed antenna five peak resonant frequencies at (a) 2.31 GHz, (b) 4.85 GHz, (c) 8.33 GHz, (d) 12.11 GHz and (e) 16.41 GHz.

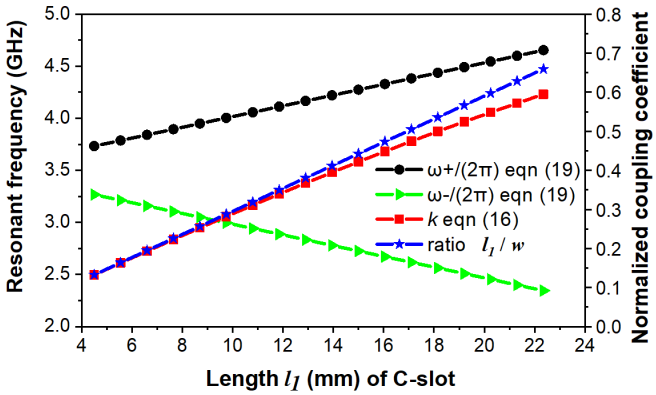

Figure 9. Variation of resonant frequency and coupling coefficient with respect to l_1 of the C-slot keeping all other dimensions constant.

According to Eq. (15), the larger the difference between resonant frequencies is, the greater the coupling coefficient is. The ratio of the slot length l_1 to the rectangular patch width w (i.e., l_1/w) controls the coupling coefficient due to the fraction of the TM_{01} mode current intercepted by the slot. It is observed from the ratio analysis that the greater the value of l_1 is, the more difference the resonant frequencies are. This performance is presented in Figure 9 for the proposed antenna varying only l_1 while all other parameters remain constant. From Figure 9, the first-order approximation of k (Eq. (16) using the CMT resonant frequencies) is

$$k \sim l_1/w \tag{18}$$

Combining Eqs. (15) and (17) with $\omega_1 = \omega_2$, we have

$$\omega_{\pm} = \omega_o \left(1 \pm l_1/(2w)\right) \tag{19}$$

Equation (19) represents the relationship between the coupled mode frequencies and uncoupled mode frequencies derived from the CMT. Depending on the frequency, the surface current distributions of the C-shaped slots and rectangular patch edges have in-phase and anti-phase relationships. From Figure 8, it is observed that at the point of contact, i.e., at feedline and patch, the direction of surface current is reverse. Since surface current flows in the reverse direction, the cancelation of radiation fields produces the high attenuation near peak resonant frequencies.

Table 4. Comparison of proposed antenna with other recently reported antennas.

Ref.	Type	Dimension (mm^3)	Freq. (GHz)	FBW (%)	PG (dBi)	GV (dBi)	BDR
5	Slot antenna	$0.24 \times 0.32 \times 0.016\lambda_l^3$	3.1–10.9	111.42	−1–4	5	1450.78
7	Monopole	$0.35 \times 0.35 \times 0.006\lambda_l^3$	3.1–11	112.05	2.1–5.6	3.5	914.70
11	Monopole	$0.37 \times 0.17 \times 0.007\lambda_l^3$	1.44–18.8	172	1–7	6	2734.50
13	Slot antenna	$0.80 \times 0.80 \times 0.009\lambda_l^3$	2.83–18.2	146	2–6.5	4.5	228.12
14	Slot antenna	$0.88 \times 0.88 \times 0.006\lambda_l^3$	3.7–19.3	135	−1–4.5	5.5	174.32
17	Monopole	$0.25 \times 0.28 \times 0.001\lambda_l^3$	3–11	114	−0.2–3.5	3.7	1727.78
18	Slot antenna	$0.24 \times 0.29 \times 0.007\lambda_l^3$	2.9–11.8	121	2–6	4	1738.50
20	Monopole	$0.39 \times 0.24 \times 0.005\lambda_l^3$	0.28–2.27	156.1	0.12–5.57	5.45	1667.73
Work	Slot antenna	$0.23 \times 0.22 \times 0.004\lambda_l^3$	1.55–16.95	166.51	2–8.3	6.3	3290.71

FBW: Fractional bandwidth. PG: Peak gain. GV: Gain variation. BDR: Bandwidth dimension ratio.

3.3. Bandwidth Dimension Ratio (BDR)

The antenna bandwidth dimension ratio (BDR) [11], which is defined as the amount of percentage bandwidth (%BW) with respect to the electrical length and width of the proposed antenna at lower sideband frequency, is expressed below:

$$\mathrm{BDR} = \frac{\%\mathrm{BW}}{\lambda_{LfL}\lambda_{WfL}} \tag{20}$$

where λ_{LfL} and λ_{WfL} are the electrical length and width of the proposed antenna at lower band frequency that meets -10 dB impedance bandwidth. The larger the value of BDR is, the smaller the dimension is and the wider the impedance bandwidth is. A very excellent BDR value, i.e., 3290.71, is observed, and the detailed comparison is given in Table 4.

4. TLM-RLC CIRCUIT MODEL OF THE PROPOSED ANTENNA

The development of an electrical equivalent circuit diagram of the proposed antenna assuring that TLM-RLC model is shown in Figure 10. In this figure, the inductance L_R is introduced by the microstrip feed line as shown in Figure 10(a). To draw the TLM-RLC circuit of the simple CPW-fed patch, the patch is considered as a parallel plate transmission line connecting radiating slots as shown in Figure 10(b). The shunt capacitances C_{R1} and C_{R2} are the gaps between the feed line and CPW-fed ground plane of both sides. The C-shaped slot considering a combination of three rectangular slots (one vertical slot and two horizontal slots) is represented in Figure 10(c). The proposed antenna contains symmetrical

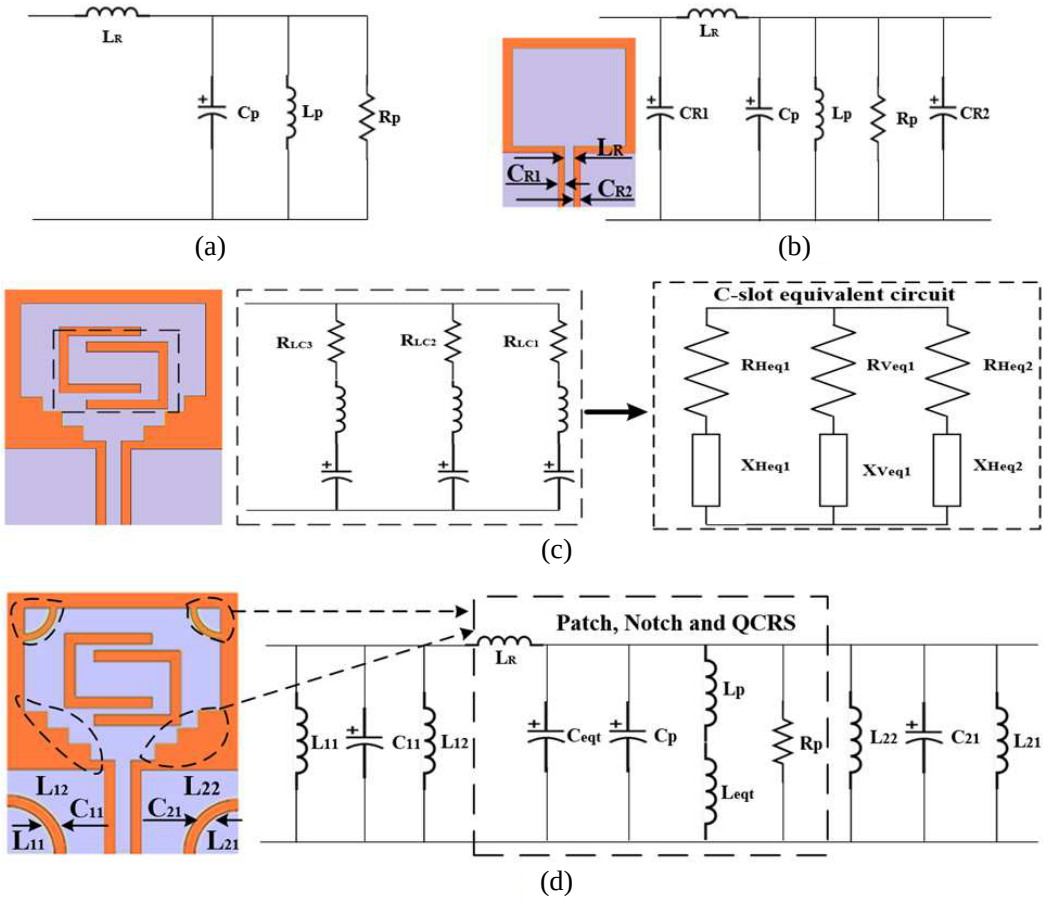

Figure 10. Equivalent transmission line model (TLM)-RLC circuit elements of proposed antenna. (a) basic patch antenna, (b) basic patch with CPW-fed, (c) C-shaped slot and (d) patch, notch, and QCRS.

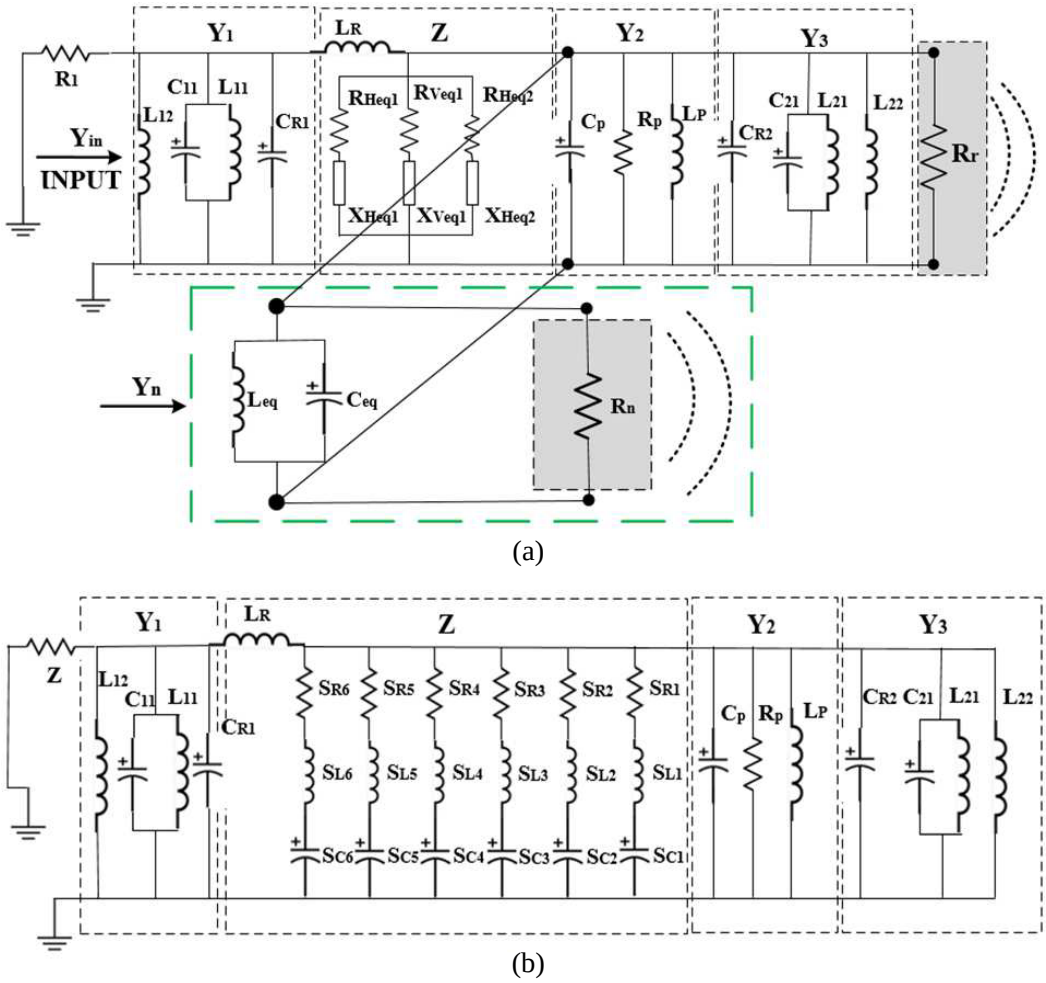

Figure 11. Equivalent transmission line model (TLM)-RLC circuit model of the proposed antenna. (a) equivalent circuit model, (b) simplified circuit model with RLC values [$L_R = 0.362$, $L_{11} = 5050$, $L_{12} = 233 \times 10^{-3}$, $L_p = 253$, $L_{21} = 14.56$, $L_{22} = 15.08$, $S_{L1} = 1.03$, $S_{L2} = 1.47$, $S_{L3} = 1.54$, $S_{L4} = 1.06$, $S_{L5} = 1.36$, $S_{L6} = 1.35$] all dimensions are in nH, [$C_{11} = 2.09 \times 10^{-12}$, $C_p = 1.2 \times 10^{-11}$, $C_{21} = 0.0124$, $C_{R1} = 0.0957$, $C_{R2} = 0.0042$, $S_{C1} = 8.5 \times 10^{-5}$, $S_{C2} = 0.01931$, $S_{C3} = 1.24 \times 10^{-5}$, $S_{C4} = 0.0011$, $S_{C5} = 0.0005$, $S_{C6} = 0.051$] all dimensions are in pF and [$Z = 50$, $R_p = 365$, $S_{R1} = 1.75$, $S_{R2} = 1.6$, $S_{R3} = 1.94$, $S_{R4} = 2.12$, $S_{R5} = 1.55$, $S_{R6} = 2.31$] all dimensions are in Ω.

staircase-shaped notches and two pairs of QCRSs as shown in Figure 10(d). Furthermore, C_{11}, C_{eqt}, and C_{21} are the coupling capacitors, while L_{11}, L_{12}, L_{eqt}, L_{21}, and L_{22} are the inductors on both sides of the symmetric ground plane.

The simplified TLM-RLC circuit model is shown in Figure 11(a). An optimization process is performed by using the NI AWR simulator, and all parameters values are labeled in Figure 11(b) (R in (Ω), C in (pF), and L in (nH)). Therefore, the impedance (Z) of the final simplified TLM-RLC equivalent circuit is given by:

$$Z = \frac{1}{G_{TC} + jB_{TC}} + j\omega L_R \tag{21}$$

The admittance Y_{Heq1} of the horizontal slot equivalent circuit is given by:

$$Y_{Heq1} = \frac{1}{R_{Heq1} + jX_{Heq1}} = G_{1C} + jB_{1C} \tag{22}$$

The admittance Y_{Veq1} of the vertical slot equivalent circuit is given by:

$$Y_{Veq1} = \frac{1}{R_{Veq} + jX_{Veq}} = G_{2C} + jB_{2C} \tag{23}$$

Similarly, the admittance Y_{Heq2} of the horizontal slot equivalent circuit is given by:

$$Y_{Heq2} = \frac{1}{R_{Heq2} + jX_{Heq2}} = G_{3C} + jB_{3C} \tag{24}$$

Hence, the total conductance G_{TC} and susceptance B_{TC} are given as follows:

$$G_{TC} = G_{1C} + G_{2C} + G_{3C} \quad B_{TC} = B_{1C} + B_{2C} + B_{3C} \tag{25}$$

The total admittance Y_C of C-slot and feed-line L_R of the proposed antenna is given by:

$$Y_C = 1/Z \tag{26}$$

The total admittance Y of the final proposed antenna of an electrical equivalent circuit is given by:

$$Y = Y_1 + Y_2 + Y_3 + Y_C \tag{27}$$

where Y_1, Y_2, and Y_3 are

$$Y_1 = j\left(\omega C_{R1} + \omega C_{11} - \frac{L_{11} + L_{12}}{\omega L_{11} L_{12}}\right) \tag{28}$$

$$Y_2 = R_p + j\omega C - \frac{j}{\omega L} \tag{29}$$

$$Y_3 = j\left(\omega C_{R2} + \omega C_{21} - \frac{L_{21} + L_{22}}{\omega L_{21} L_{22}}\right) \tag{30}$$

where $C = C_p \parallel C_{eqt}$ and $L = L_p \parallel L_{eqt}$.

Figure 11(a) shows an LC circuit model of Antenna 5 (proposed) and explains how the center frequencies, and the bandwidths can be controlled by an LC circuit of the notched structure. The radiation resistance of the antenna element and the notch are R_r, R_n, respectively. L_{eq} and C_{eq} represent an inductor and capacitor of the notch resonator circuit. The notch admittance Y_n of the parallel RLC resonator circuit is given by [27]:

$$Y_n = \frac{1}{R_n} + j\omega C_{eq} + \frac{1}{j\omega L_{eq}} \tag{31}$$

$$Y_{in} = Y + \frac{1}{R_r} + \frac{J_1^2}{Y_n} \tag{32}$$

where J_1 is the Bessel function of the parallel RLC resonator circuit, and its resonant frequency is given by:

$$\omega_o = \frac{1}{\sqrt{L_{eq} C_{eq}}} \tag{33}$$

Putting Eq. (33) in Eq. (31) with $\omega = \omega_o + \Delta\omega$, Eq. (31) is reduced to

$$Y_n = \frac{1}{R_n} + \frac{j}{\omega L_{eq}}\left(\omega^2 L_{eq} C_{eq} - 1\right) \approx \frac{1}{R_n} + j2C_{eq}\Delta\omega \tag{34}$$

The bandwidth of the RLC parallel resonant circuit approximately equals twice the -3 dB bandwidth of the parallel R_n and $2C_{eq}$ as shown in Eqs. (35) and (36). Here, the fractional bandwidth (FBW) represents [19]:

$$\text{BW} = \frac{2}{R_n \times 2C_{eq}} = \frac{1}{R_n C_{eq}} \tag{35}$$

$$\text{FBW} = \frac{\text{BW}}{\omega_o} = \frac{1}{\omega_o R_n C_{eq}} \tag{36}$$

Finally, the proposed UWB antenna model gives approximately the same behaviour, and a very wide impedance bandwidth is constituted by several adjacent resonances which can be represented by TLM-RLC circuits simulated result as shown in Figure 12.

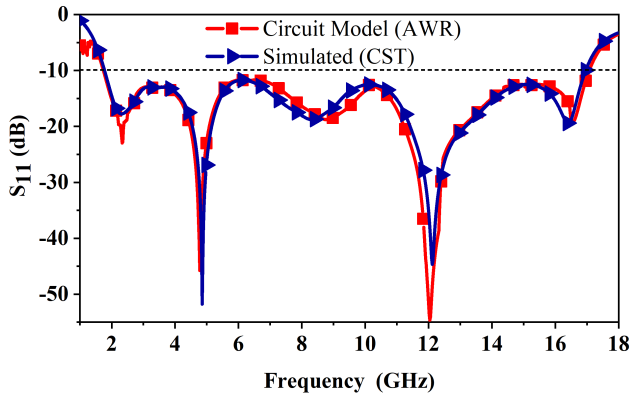

Figure 12. Simulated and equivalent transmission line circuit model response of the proposed antenna.

5. SIMULATION AND MEASUREMENT RESULTS

The prototype of the proposed antenna is shown in Figure 13(a). The performance of S_{11} is measured with a vector network analyzer (Rohde and Schwarz ZVA24). The peak gain, efficiency, and radiation patterns are measured with an antenna measurement environment for 1–18 GHz band in an anechoic chamber (size: $6 \times 4 \times 6\,\mathrm{m}^3$) as shown in Figure 13(b).

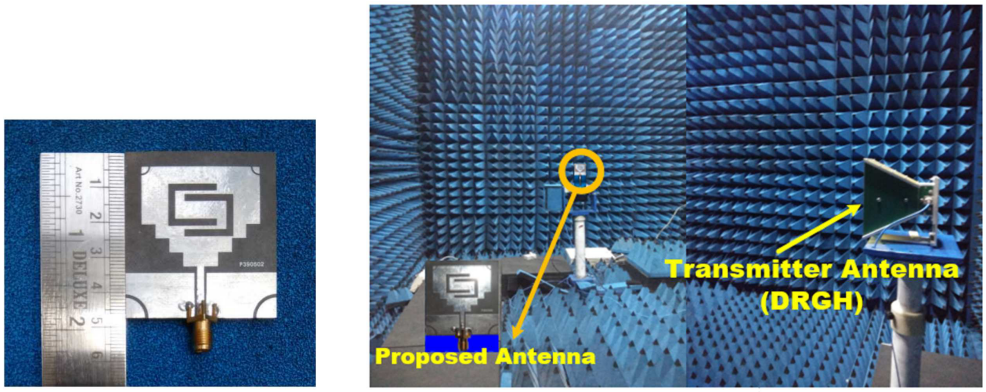

(a) (b)

Figure 13. (a) Photograph of the prototype UWB antenna and (b) actual antenna measurement environment setup.

5.1. Reflection Coefficient S_{11}

The measured and simulated S_{11} parameters of the proposed antenna are shown in Figure 14. The inset figure shows a photograph of the fabricated antenna. The measured results show a very wide impedance bandwidth from 1.55 to 16.95 GHz (percentage of the bandwidth 166.51%) with a bandwidth ratio of 10.94 : 1. The simulated results obtained using the CST simulator closely match the measured ones for the entire operating band. The small difference in the lower sideband, as well as the higher sideband, is mainly due to the fabrication tolerance.

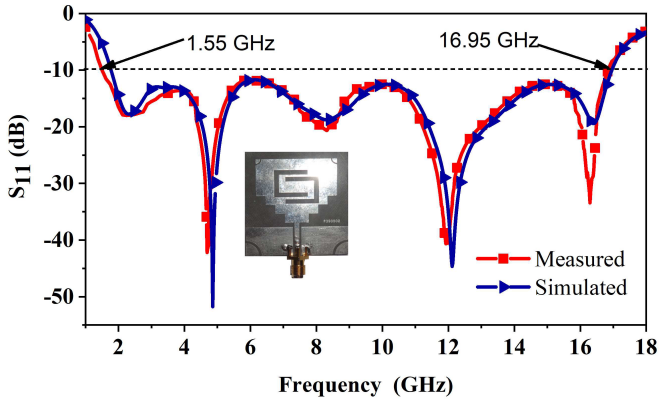

Figure 14. Measured and simulated S_{11} performance of the proposed UWB antenna.

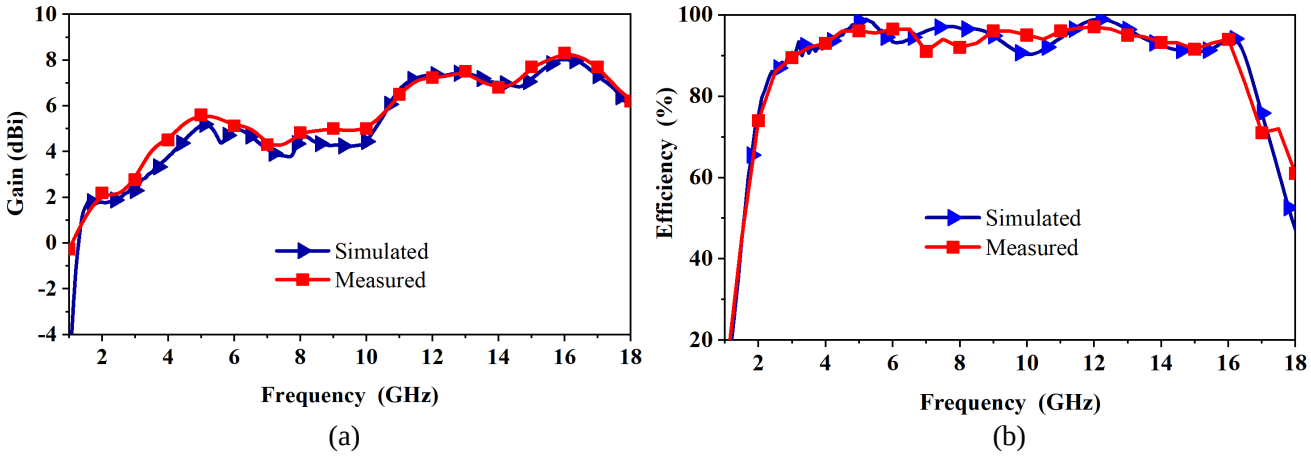

Figure 15. Measured and simulated of the proposed UWB antenna, (a) peak gain and (b) efficiency.

5.2. Gain and Efficiency

The gain of the presented antenna simulated using the CST simulator and compared with the measured results is shown in Figure 15(a). It is seen that the measured gain closely matches the simulated results over the operating band. The peak gain varies from 2 to 8.3 dBi with the increase of frequency up to 17 GHz. For efficiency measurement, at first measure the peak gain, radiation intensity, and reflection coefficient. The directivity is computed automatically using the radiation intensity, and all calculation is done using the software. The antenna efficiency is computed using the equation given below:

$$\text{Efficiency} = \frac{G(\theta, \phi)}{D(\theta, \phi)} \left(1 - |\Gamma|^2\right) \tag{37}$$

The radiation efficiency performance is shown in Figure 15(b). The measured efficiencies from 1 to 17 GHz are about 82%–96%, and a little deviation from the simulated result is due to the fabrication tolerance.

5.3. Radiation Performance

The simulated and measured radiation patterns of the proposed antenna in E- and H-planes at 1.55, 2.31, 4.85, 8.33, 12.11, and 16.95 GHz are shown in Figures 16(a) and 16(b), respectively. The measured results nearly match the simulated ones in both cases of E-plane (yz plane) and H-plane (xz plane). Figures 16(a) and 16(b) show that the antenna radiates equally in both x-directions (i.e., positive x-axis

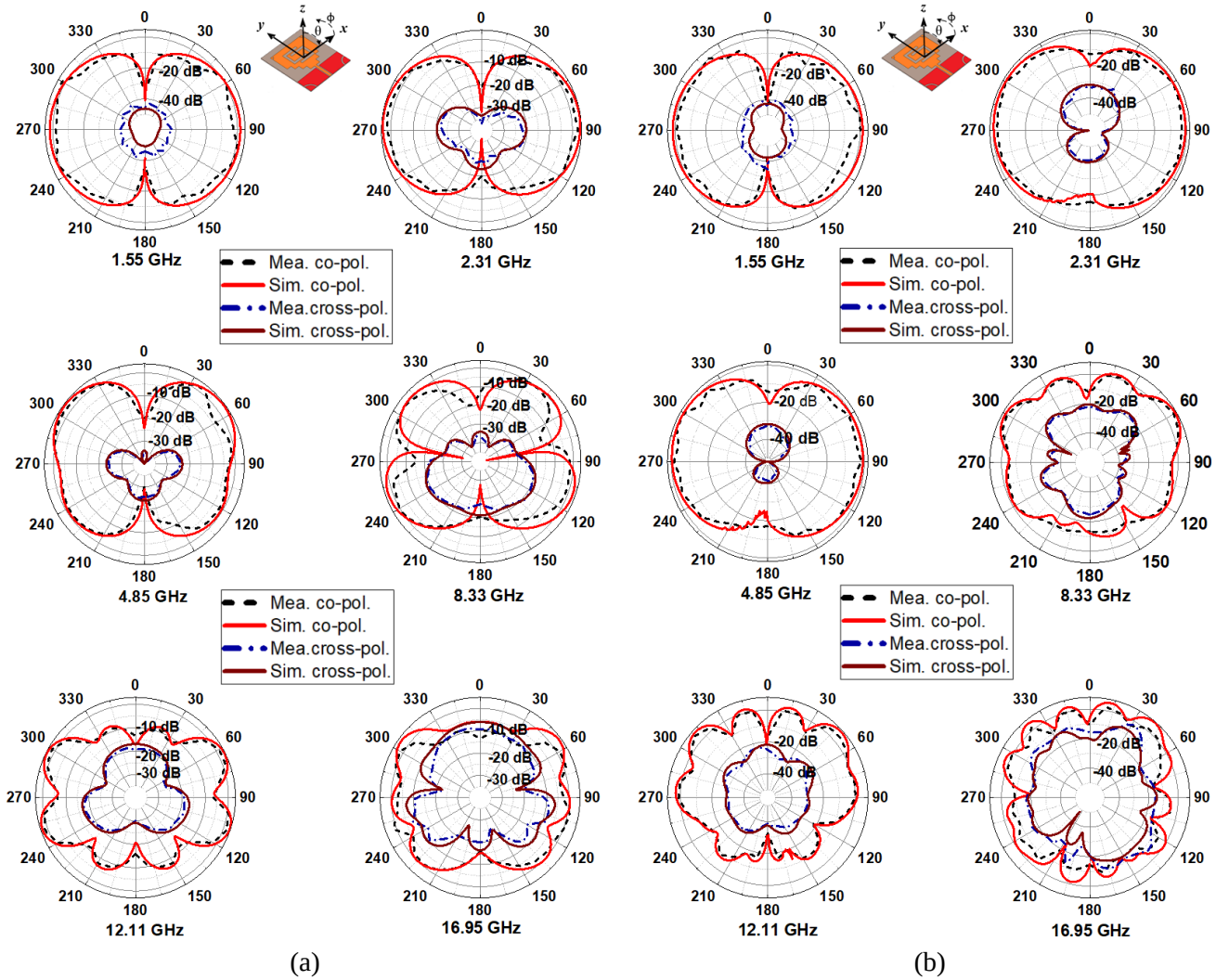

Figure 16. Measured (dashed curve) and simulated (solid curve) radiation patterns of the proposed antenna at 1.55, 2.31, 4.85, 8.33, 12.11 and 16.95 GHz, (a) E-plane (yz plane) and H-plane (xz plane).

and negative x-axis) and does not change the radiation patterns shape with increase of frequency. The simulated and measured radiation patterns show that the cross-polarization is about 20 dBi lower than the co-polarization value at the boresight of the designed antenna in all cases where with the E-plane at 16.95 GHz, the cross-polarization and co-polarization values have less difference. The measured results indicate that the proposed antenna has stable and nearly omnidirectional radiation patterns in the UWB.

Table 4 gives the comparison performances between the proposed symmetrical staircase-shaped UWB antenna and other UWB antennas proposed in the literature. The antenna type, dimension, frequency range, fractional bandwidth (% BW), peak gain, and bandwidth dimension ratio (BDR) are listed. The measured peak gain of the UWB antenna is greater than 2 dBi and reaches up to 8.3 dBi within the -10 dB impedance band. Table 4 demonstrates the effectiveness of the proposed structure in obtaining enhanced impedance bandwidth, better gain, and good radiation performance with a compact size. The proposed antenna has a smaller size than most of the literature but still maintains a wider impedance bandwidth. Besides, the bandwidth dimension ratios (BDRs) in all the listed types have low value, whereas the proposed antenna has a very high value, i.e., 3290.71, which indicates a small size. Therefore, considering all the performance of the proposed antenna, it will be a good candidate for UWB applications.

6. CONCLUSION

In this work, a simple symmetrical staircase-shaped UWB antenna with wider impedance bandwidth over a 1.55 to 16.95 GHz (fractional BW = 166.51%) band is presented. From the comparison of the BDR, it is observed that the BDR of the proposed antenna is higher than the other antennas proposed in literature. The comparison in terms of BDR verifies the advantages of compact size and wider bandwidth provided by the proposed antenna structure than other antenna structures. Owing to the advantages of compact size and wider bandwidth than other antenna structures, this antenna will be useful for UWB application, mobile applications, wireless applications, satellite applications, radio determination applications (4.5–7 GHz and 13.4–14 GHz), etc. Finally, an electrical equivalent TLM-RLC circuit of the design UWB antenna is presented based on the effect of each slot and antenna elements. The simulated results of the TLM-RLC circuit model are nearly the same as the designed antenna results obtained from the CST simulator software.

ACKNOWLEDGMENT

This work is supported by Impacting Research Innovation and Technology (IMPRINT II) by MHRD and DST, India. Project No. IMP/2018/001179/SD.

REFERENCES

1. Molisch, A. F., K. Balakrishnan, D. Cassioli, C.-C. Chong, S. Emami, A. Fort, J. Karedal, J. Kunisch, H. Schanntz, and K. Siwiak, "A comprehensive model for ultrawideband propagation channels," *Proc. IEEE Global Telecommun. Conf. (GLOBECOM)*, 3648–3653, 2005.
2. Porcino, D. and W. Hirt, "Ultra-wideband radio technology: Potential and challenges ahead," *IEEE Commun. Mag.*, 66–74, Jul. 2003.
3. *FCC First Report and Order on Ultra-wideband Technology*, Document FCC 02-48, Feb. 2002.
4. Chiu, S. C. and S. Y. Chen, "Miniaturization of CPW-fed slot antenna using a pair of interdigital capacitors," *Proc. IEEE Antennas Propag. Soc. Int. Symp., (APSURSI)*, 1380–1381, Orlando, FL, USA, Jul. 2013.
5. Orazi, H. and H. Soleiman, "Miniaturisation of UWB triangular slot antenna by the use of DRAF," *IET Microw. Antennas & Propag.*, Vol. 11, No. 4, 450–456, Feb. 2017.
6. Sallam, M. O., S. M. Kandil, V. Volski, G. A. E. Vandenbosch, and E. A. Soliman, "Wideband CPW-fed flexible bow-tie slot antenna for WLAN/WiMAX systems," *IEEE Trans. Antennas Propag.*, Vol. 65, No. 8, 4274–4277, Aug. 2017.
7. Safia, O. A., M. Nedil, L. Talbi, and K. Hettak, "Coplanar waveguide-fed rose-curve shape UWB monopole antenna with dual-notch characteristics," *IET Microw. Antennas & Propag.*, Vol. 12, No. 7, 1112–1119, Jan. 2018.
8. Azari, A., "A new super wideband fractal microstrip antenna," *IEEE Trans. Antennas Propag.*, Vol. 59, No. 5, 1724–1727, May 2011.
9. Tu, Z.-H., W.-A. Li, and Q.-X. Chu, "Single-layer differential CPW-fed notch-band tapered-slot UWB antenna," *IEEE Antennas Wireless Propag. Lett.*, Vol. 13, 1296–1299, May 2014.
10. Tasouji, N., J. Nourinia, C. Ghobadi, and F. Tofigh, "A novel printed UWB slot antenna with reconfigurable band-notch characteristics," *IEEE Antennas Wireless Propag. Lett.*, Vol. 12, 922–925, Jun. 2013.
11. Chen, K.-R., C. Y. D. Sim, and J.-S. Row, "A compact monopole antenna for super wideband applications," *IEEE Antennas Wireless Propag. Lett.*, Vol. 10, 488–491, Apr. 2011.
12. Fang, X., G. Wen, D. Inserra, Y. Huang, and J. Li, "Compact wideband CPW-fed meandered-slot antenna with slotted Y-shaped central element for Wi-Fi, WiMAX, and 5G applications," *IEEE Trans. Antennas Propag.*, Vol. 66, No. 12, 7395–7399, Dec. 2018.
13. Dastranj, A. and H. Abiri, "Bandwidth enhancement of printed E-shaped slot antennas fed by CPW and microstrip line," *IEEE Trans. Antennas Propag.*, Vol. 58, No. 4, 1402–1407, Apr. 2010.

14. Moghadasi, M. N., A. Danideh, R. Sadeghifakhr, and M.-R. Azadi, "CPW-fed ultra wideband slot antenna with arc-shaped stub," *IET Microw. Antennas & Propag.*, Vol. 3, No. 4, 681–686, Sept. 2009.
15. Liu, H., S. Zhu, P. Wen, X. Xiao, W. Che, and X. Guan, "Flexible CPW-fed fishtail-shaped antenna for dual-band applications," *IEEE Antennas Wireless Propag. Lett.*, Vol. 13, 770–773, Apr. 2014.
16. Wu, J., Z. Zhao, Z. Nie, and Q. Liu, "A printed UWB Vivaldi antenna using stepped connection structure between slotline and tapered patches," *IEEE Antennas Wireless Propag. Lett.*, Vol. 13, 698–701, Apr. 2014.
17. Eshtiaghi, R., J. Nourinia, and C. Ghobadi, "Electromagnetically coupled band-notched elliptical monopole antenna for UWB applications," *IEEE Trans. Antennas Propag.*, Vol. 58, No. 4, 1397–1402, Apr. 2010.
18. Yang, Y., Z. Zhao, X. Ding, Z. Nie, and Q.-H. Liu, "Compact UWB slot antenna utilizing traveling-wave mode based on slotline transitions," *IEEE Trans. Antennas Propag.*, Vol. 67, No. 1, 140–150, Jan. 2019.
19. Dong, Y. D., W. Hong, Z. Q. Kuai, and J. X. Chen, "Analysis of planar ultrawideband antennas with on-ground slot band-notched structures," *IEEE Trans. Antennas Propag.*, Vol. 57, No. 7, 1886–1893, Jul. 2009.
20. Ashong, E. T. and Y.-B. Jung, "Bandwidth enhancement and size reduction of printed monopole antenna using bounding box structure," *IET Microw. Antennas & Propag.*, Vol. 13, No. 9, 1484–1490, Apr. 2019.
21. Katyal, A. and A. Basu, "Analysis and optimisation of broadband stacked microstrip antennas using transmission line model," *IET Microw. Antennas & Propag.*, Vol. 11, No. 1, 81–91, Feb. 2017.
22. Amro, W. H. A. A. and M. K. Abdelazeez, "Analysis and optimisation of super-wideband monopole antenna with tri-band notch using a transmission line model," *IET Microw. Antennas & Propag.*, Vol. 13, No. 9, 1373–1381, Jun. 2019.
23. Pierce, J. R., "Coupled modes," *Almost All About Waves*, Ch. 6, 47, MIT Press, 1974.
24. Haus, H. A. and W. Huang, "Coupled-mode theory," *Proceedings of the IEEE*, Vol. 79, No. 10, 1505–1518, Oct. 1991.
25. Chuang, S. L., "Waveguide couplers and coupled mode theory," *Physics of Optoelectronic Devices*, 1st Edition, Ch. 8, Sec. 2.2, 291, Wiley, New York, NY, USA, 1995.
26. Hong, J.-S., "Couplings of asynchronously tuned coupled microwave resonators," *IEEE Proceedings — Microwaves, Antennas and Propagation*, Vol. 147, No. 5, 354–358, Oct. 2000.
27. Liu, S., S. S. Qi, W. Wu, and D. G. Fang, "Single-layer single-patch four-band asymmetrical U-slot patch antenna," *IEEE Trans. Antennas Propag.*, Vol. 62, No. 9, 4895–4899, Sept. 2014.
28. Balanis, C. A., *Antenna Theory*, 811–882, John Wiley & Sons, INC, Hoboken, 2005.